Eur. Phys. J. Special Topics **177**, 41–57 (2009)

DOI: 10.1140/epjst/e2009-01167-6

THE EUROPEAN PHYSICAL JOURNAL SPECIAL TOPICS

Regular Article

Atomistic calculations on interfaces: Bridging the length and time scales

A tutorial review

L. Lymperakis[a], M. Friák, and J. Neugebauer

Computational Materials Design Department, Max-Planck-Institut für Eisenforschung GmbH, Max-Planck-Straße 1, Düsseldorf, Germany

Abstract. Phase field simulations suitable to describe interfacial phenomena at the mesoscale require as input parameters accurate interfacial energies as well as the interface mobilities. However, this information is not directly accessible by experiment. Furthermore, phenomena such as impurity segregation cannot be decoupled and their independent role in interfacial cohesion and mobility cannot be deduced. On the other hand *ab-initio* calculations and/or classical interatomic potentials are suitable tools which can provide an on-atomic-scale description of the interfaces. However, there are a number of challenges that one encounters: multidimensional phase space of the interfacial misorientation degrees of freedom, suitable driving forces, and large length and time scales just to mention a few. In the present report we provide an extended review on the atomistic calculations and the simulation strategies proposed to tackle the corresponding problems.

1 Introduction

Phase field simulations are by now well established as an important tool in the computational physical metallurgy which may describe phenomena associated with microstructural evolution such as dendritic growth, martensitic and other phase transitions as well as grain growth [1]. A prerequisite for phase field simulations is the accurate knowledge of material specific parameters such as solid–solid and solid–liquid interface energies and the corresponding kinetic parameters. In most cases this information is not always directly accessible by experiment. For example the experimentally derived interfacial energies as well as interfacial mobilities always include the influence of small amount of impurities: Even tiny concentrations of them may drastically alter the corresponding properties. In order to control the microstructural evolution a detailed understanding of those phenomena is required. Thus, methods which will allow for a full control over all system parameters such as interfacial symmetries, impurity concentrations, segregation effects, or pressure and temperature are required.

Atomistic calculations based on first-principles and/or empirical potentials satisfy the aforementioned requirements and are widely used to describe interfacial as well as interphasial phenomena. In a bottom-up simulation hierarchy both approaches are with respect to length and time scale below the phase field simulations with length scales ranging up to a few hundreds of nanometers for empirical potential based calculations. First-principles calculations are free of empirical or other fitting parameters, are transferable (i.e. can accurately describe different environments) and can be applied to multicomponent alloy systems. However, they are suffering from their extensive requirements on memory and CPU power and they thus are restricted to

[a] e-mail: lymperakis@mpie.de

rather small system sizes ranging up to a few nanometers length scales. On the other hand empirical potentials can be extended to larger length and time scale but their transferability and accuracy should always be checked and ensured in advance.

In the following sections we will focus and review on atomistic calculations of the static properties of Solid–Solid and Solid–Liquid interfaces. In the first section we will provide a short discussion on the atomistic calculations. In the two subsequent sections we will discuss the Solid–Solid interfaces: In Section 3 we will focus on a specific subclass of grain boundaries, the coherent interphase boundaries and we will briefly discuss the atomistic approaches to tackle the corresponding problems. The grain boundaries will be the topic of Section 4. In the last section we will review the different approaches to simulate Solid-Liquid interfaces and calculate the interfacial energy and stiffness.

2 Atomistic simulations

Computer simulations have been emerged as an important branch in the field of materials science and engineering over the last few decades. From a conceptual point of view computer simulations link theory with experiment. Atomistic simulations (molecular dynamics or Monte Carlo simulations) is a term which refers to those simulation techniques and models where atoms are the building blocks of the systems under consideration. Those techniques has been and are used for studying various systems ranging from atoms and small molecules and clusters to large biomolecules, crystals, surfaces, interfaces, or liquid systems.

Atomistic simulations can in principle be categorized in two groups depending on whether empirical input data are used. In the first class we find the *ab-initio* (first-principles) calculations: The treatment of the system is based solely on quantum mechanical concepts and in principle no-empirical parameters enter. On the other hand in the empirical and/or semi-empirical methods approximate interatomic interactions which depend on a group of parameters obtained by empirical and/or *ab-initio* data are used.

A detailed review of *ab-initio* and the empirical potential calculations is beyond the scope of the present review. Nevertheless in the following paragraphs we will shortly present the ideas underlying both simulation techniques along with a small discussion on the advantages and the applicability of them.

2.1 First-principles calculations

The principle idea underlying the first-principles calculations is to assume any many-atom system as a many-body system consisting of electrons and nuclei and treat them on the basis of quantum mechanical concepts. Nevertheless, in most cases in materials science the quantum behavior of the nuclei is not important and thus they can be regarded as classical particles. Moreover, as Born and Oppenheimer noted in 1923, the nuclei are much more massive than the electrons and move on a time scale which is approximately two orders of magnitude larger than that of the electrons. Thus, the electrons can respond to the ionic motion almost instantaneously and any change in the electronic state occurs vary rapidly compared to the nucleus motion. Therefore, it is a good approximation to separate electronic and ionic motion and to perform the calculation of the electronic structure separately from the calculation of the ionic motion. On the other hand electrons must be described by quantum mechanics in any situation. The electronic Hamiltonian consisting of system of N_e electrons and N_I nuclei, neglecting relativistic effects, can be written as:

$$H_e = \sum_{i}^{N_e} \left[-\frac{1}{2}\nabla_i^2 \right] - \sum_{i}^{N_e} \sum_{I}^{N_I} \left[\frac{Z_I}{|r_i - R_I|} \right] + \frac{1}{2} \sum_{i}^{N_e} \sum_{i'}^{N_{i'}} \left[\frac{1}{|r_i - r_i'|} \right], \tag{1}$$

where R_I and Z_I are the position and the atomic number of the nucleus I respectively, and r_i is the position of the electron i.

There are three different classes of quantum mechanical approaches to determine the ground state of many body systems: The simplest of the *ab-initio* methods is the Hartree–Fock (HF) approximation (see pp 11–18 in Ref. [72]). The HF approximation replaces the N_e electron wavefunction by a antisymmetric wavefunctions having the form of a Slater determinant. The ground state energy is determined by invoking the variational principle. However, the HF approximation has the disadvantage that it cannot describe the electronic correlation properly. For example it gives zero density of states at the Fermi level of metals.

Alternatively to the HF approximation, one may consider the Density Functional Theory (DFT). In DFT the many-body problem is reformulated in terms of the electron density ρ [71, 89]. Electron density compared to the many-body wavefunction is more attractive, since it drastically reduces the degrees of freedom: it depends only on x, y, and z spatial coordinates and there may be two densities for spin polarized systems: $\rho\uparrow$ (spin up) and $\rho\downarrow$ (spin down). In contrast, the many-body wavefunction depends on all coordinates of all particles. Although, DFT originally applied in atoms and simple molecules, nowadays can be assumed as a work horse for more complex systems in the chemical and materials sciences. The interesting reader is referred to the excellent reviews on DFT in Refs. [71,72].

Unlike the single particle HF and DFT approximations, Quantum Monte Carlo (QMC) approaches use statistical techniques to solve the many dimensional integrals and model many-body wavefunction directly [90]. The great significance of QMC techniques is that they are relatively insensitive to the dimensionality of the problem. This advantage allows the study of systems which are typically beyond the reach of other approaches. However, QMC methods suffer from the fact that their accuracy improves only slowly with the computational resources used.

Ab-initio based methods provide a reliable tool for accurate atomic scale calculations. However, a major drawback of DFT calculations is their rather limited ability to represent systems consisting of large numbers of atoms and/or to perform simulations over a large timescale, in the case of Molecular Dynamics (MD). Thus, it is crucial to develop and introduce numerically simpler methods that will allow to treat large scale systems and/or long time scale simulations. An established method to do this is the application of empirical potentials (EP).

2.2 Empirical interatomic potentials

One of the first pair potentials used in atomistic simulations is the hard spheres model. It consists of an pair potential of the following form:

$$\Phi_{12} = \begin{cases} \infty, \, r < \sigma \\ 0, \;\; r \geq \sigma \end{cases} \tag{2}$$

where Φ_{12} is the pair interaction between two spheres at a distance r, and σ is the diameter of the sphere. The hard spheres potential models the interaction between impenetrable spheres that cannot overlap. It has been widely used to study the thermodynamics of solid and liquid systems, phase transitions, and solid-liquid interfaces.

One of the most widely used pair potentials in atomistic calculations is the Lennard–Jonnes (LJ) model. The analytical form of the LJ pairwise interactions is the following:

$$\Phi_{12}(r) = 4\epsilon \left[\left(\frac{\sigma}{r} \right)^{12} - \left(\frac{\sigma}{r} \right)^{6} \right], \tag{3}$$

where σ and ϵ are the specific LJ parameters, different for different interacting particles. σ is the length at which the interaction vanishes ($\Phi_{12} = 0$) and ϵ is the depth of the potential well. For large separation distances r the $1/r^6$ term dominates and the LJ potential is attractive. This behaviour represents the London dispersion forces. However, as the separation distance decreases the $1/r^{12}$ dominates and the potential becomes repulsive.

Apart from the simple pairwise potentials, more sophisticated and more complex many-body potentials have been developed in order to incorporate the influence of the local environment

of each atom into the energy of the system. Among the most popular many-body potentials are the Finis-Sinclair (FS) [91] and embedded atom method (EAM) [92,93] potentials. The main idea behind these models is that the strength of the chemical bond depends both on the interatomic distance as well as the bonding environment. They consist of a pair potential term which is modified by an environmental dependent many-body term. The analytical function of the 2nd nearest neighbors modified EAM type potentials has for example the following form:

$$E = \sum_i \left[F\left(\overline{\rho}_i\right) + \frac{1}{2} \sum_{j \neq i} \phi\left(R_{ij}\right) \right] \tag{4}$$

where $\phi(R_{ij})$ is an attractive pair potential and $F\left(\overline{\rho}\right) = AE_c \left(\overline{\rho}/\overline{\rho}^0\right) \ln\left(\overline{\rho}/\overline{\rho}^0\right)$ is the embedding energy function which incorporates the effects of the local environment. The dependence on the environment enters through the background electron density $\overline{\rho}_i$ at the atomic position r_i formed by the surrounding atoms sitting on positions r_j. ρ^0 is the electron background density for the reference structure, E_c is the sublimation energy, and A is an adjustable parameter. Various parametrizations of the FS and EAM type potentials have been proposed over the last decades to model various single element such as Al, Cu, Ag, Au, Ni, Pd, Pt, and Pb [98], just to mention a few as well as for multicomponent systems such as ternary C-Fe alloys [99] and quaternary Ni-Al-H systems [97]. A detailed database and documentation of EAM and FS potentials can be found at the NIST online repository [100].

2.3 Discussion on the atomistic calculations

Ab-initio methods are by now a well established tool for accurate, parameter free simulations in the field of materials science and engineering. Their range of applications varies from total energy and electronic structure calculations of small molecules and cluster, to crystals, point defects, and extended defects, just to mention a few. However, they suffer from their extensive demands on computational resources. The CPU time required to calculated the ground state of a system may vary from a few hours for systems consisting of a few atoms, up to a few weeks for a few hundreds of atoms. The corresponding time scale for Molecular Dynamic calculations is limited in the order of 10^{-12} sec.

Interatomic empirical potentials have much lower demands on both CPU power and memory requirements: Calculations of systems consisting of a few millions of atoms and in a time scale of 10^{-9} sec are feasible nowadays. However, the empirical potentials are models which have there own materials properties: They are parameterized and fitted to reproduce certain material properties such as lattice parameters, elastic constants, cohesive energies, or melting temperatures just to mention a few. The transferability of a given potential, i.e. the ability of a potential to describe various environments, is always a question which should be carefully addressed. Moreover, not all potentials are suitable for all systems: A nobel gas system may be accurately described by a LJ potential or a Stillinger-Weber [96] interaction may be suitable for tetrahedrally bonded covalent system. However, it is evident that a SW potential will probably fail to mimic a metallic system. Hence, not only the parameterization but also the choice of potential depends strongly on the system under consideration. Nevertheless we should always keep in mind that the empirical interatomic potentials are material systems themselves and should be treated like that.

3 Coherent interphase boundaries

Grain boundaries (GBs) are the central structural features in thermomechanical processes such as recovery, recrystallization, and grain growth and significantly affect the physical and mechanical properties of materials. Grain boundary engineering, i.e. optimizing the population of GBs with desirable geometry by suitable thermomechanical treatment, is nowadays an important topic in functional and structural materials design [62]. In particular, polycrystalline materials

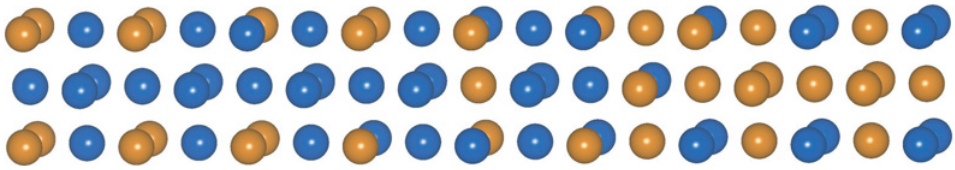

Fig. 1. Schematic drawing of a coherent interphase boundary, here between two phases with the same $L1_2$ structure (far left and far right) but the opposite composition.

characterized by relatively large number of boundaries having special misorientations are expected to exhibit exceptional macroscopic properties such as strong resistance to intergranular failure and corrosion [63,64].

A specific subclass of grain boundaries is coherent interphase boundaries (CIPBs) characterized by structural continuation of atomic planes of interfacing crystals throughout the boundary (see Fig. 1). The technological and industrial importance of CIPBs stems from the fact that one of the most efficient ways to strengthen multiphase alloys is to introduce coherent precipitates via a controlled heat treatment [2]. This treatment is referred to as the age hardening, aging, or precipitation strengthening. The effect of strengthening critically depends on the volume fraction, size, morphology, and/or spatial distribution of the precipitates. The microstructural evolution and kinetics of the precipitate formation that is determining the above mentioned parameters, decisively depend on structural and thermodynamic properties of the interphase boundaries (see e.g. a review article by Thornton et al [3]). However, experimental data are frequently not available due to difficulties in measuring the interphase boundaries. This is particularly true for multicomponent systems. Therefore, there have been several attempts to determine the most important characteristics of CIPBs, such as the interphase energy, theoretically.

3.1 Theoretical modeling of coherent interphase boundaries

The calculations of the interphase boundary energies between two immiscible phases in a binary alloy were performed using e.g. (i) the regular solution model by Lee and Aaronson [4] or (ii) the cluster variation method (CVM) by Kikuchi and Cahn [5]. In the latter, the CIPB energies in Cu-Au alloys were calculated using the sum-method approach combined with the tetrahedron approximation of the CVM (T-CVM) that unfortunately neglects longer-range interactions on the lattice. In order to take the long-range interactions into account, the tetrahedron–octahedron approximation of the CVM (TO-CVM) can be used [6,12], in which both the first and second nearest neighbor interactions are included.

As a very promising computational approach, the cluster/site approximation (CSA) was recently found to (i) possess an accuracy comparable to the CVM in phase diagram calculations, however, (ii) be much less computationally demanding [8–10]. The method was applied e.g. in [7] to determine the CIPB energies in fcc metals. Methodologically, the interphase boundary is studied by considering the thermodynamic properties of rather large systems (supercells, see Fig. 2) containing distinct spatial regions of two different bulk phases with an interface between them. Using the sum-method [6,11], the grand potential, $\Omega_{(hkl)}$, of a supercell containing e.g. a (hkl) interphase boundary in a cubic system, reads

$$\Omega_{(hkl)} = U - TS - \sum_p \mu_p N_p$$

where μ_p is the chemical potential of the p component and N_p being the total number of p atoms in the entire system. The internal energy U and configurational entropy S can be derived from different statistical mechanical models what allows for a finite temperature description.

The internal energy can be within the CSA expanded into a series of cluster probabilities and cluster energies that can be obtained from a fit to the experimental results. If the experimental

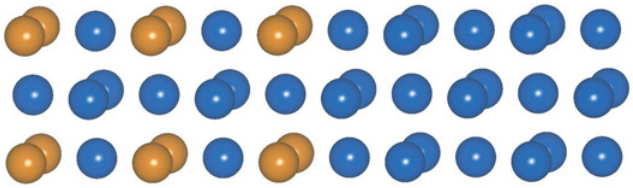

Fig. 2. Schematic drawing of a periodically repeated supercell used in the calculations of a coherent $(100)_{\mathrm{fcc}}$ interphase boundary, here between the $L1_2$ phase (left) and the fcc phase (right) with an abrupt boundary in between (mind the fact that realistic supercells contain 50 or more atomic layers [7,12]).

data are missing, *ab initio* calculations are recommended to be used in order to calculated them as such computations are essentially based on fundamental quantum mechanics and only make use of information that can be found in the periodic table, i.e. no adjustable parameters are introduced. The equilibrium state of the boundary can be obtained by minimizing the grand potential $\Omega_{(hkl)}$ for a given temperature and bulk equilibrium chemical potential. Importantly, the minimization must maintain the so-called the continuity constraints at each atomic plane (see more details in [5]).

3.2 Coherency stresses

Particularly in case of coherent interphase boundaries, a stress is often present in multiphase solids, since the lattice parameters of the different phases typically differ. These so-called coherency stresses give rise to an elastic strain energy that can affect a wide range of processes in, and equilibrium properties of, multiphase systems. Specifically, the elastic and interfacial energies can easily be comparable in systems such as high temperature alloys since these systems often possess a misfit of only up to 1%. The effect of resulting stress is small when the particles are small, however, in many alloys the particles can grow large enough such that the microstructure is decisively influenced by the presence of the elastic stresses. In addition, it can also alter (i) the diffusion coefficients [15,16], and/or (ii) particle coarsening that is significantly more complicated in a stressed environment than in a stress-free one. First, the equilibrium compositions of the coherent two-phase mixture are usually different from those determined by the incoherent phase diagrams [17]. Secondly, the elastic properties are usually anisotropic what introduces yet another level of complexity.

In the CIPB modeling, the elastic energy is taken into account either in the atomistic supercell calculations or as a contribution to the energy functional of the phase-field method (see e.g. [2,18–20]. For example, Vaithyanathan and Chen in [2] used the Khachaturyan's model for the elastic energy [21] arising from the lattice misfit with a homogeneous modulus approximation. Assuming that the lattice parameter has a linear dependence on the solute composition (Vegard's law), the elastic energy functional can be written as

$$E_{\mathrm{el}} = \frac{1}{2}\int_{\mathbf{k}} B[\mathbf{n}]|\tilde{c}(\mathbf{k})|^2 \frac{d^3\mathbf{k}}{(2\pi)^2}$$

where the integral is over the reciprocal or Fourier space, $\mathbf{n}(=\mathbf{k}/|\mathbf{k}|)$ is a unit vector in the k direction and $\tilde{c}(\mathbf{k})$ is the Fourier transform of composition field $c(\mathbf{r})$. The function $B(\mathbf{n})$ contains the information on the elasticity of the system and can be approximated in 2D [22] as

$$B(\mathbf{n}) \approx B_{\mathrm{el}}(\mathbf{n})_x^2(\mathbf{n})_y^2\varepsilon_0^2, \quad B_{\mathrm{el}} = -\frac{4(C_{11}+2C_{12})^2}{C_{11}(C_{11}+C_{12}+2C_{44})}\Delta$$

where C_{11}, C_{12} and C_{44} are independent coefficients in the elastic constant matrix, $\Delta(=C_{11}C_{12}-2C_{44})$ is the elastic anisotropy factor and $\varepsilon_0[=(\mathrm{d}a/a)(1/\mathrm{d}c)]$ is the coefficient of lattice expansion caused by the changes in composition.

In a multi-disciplinary manner, the electronic-structure calculations can be used to determine (i) thermodynamical and mechanical properties of the strained states (see e.g. [23,24]) or (ii) the elastic constants C_{ij} used in Eq. (3.2) for each of the present phases. If required by the employed model, the anisotropic elastic properties can also be homogenized into an elastically isotropic characteristic using various homogenization techniques (see e.g. [25–29]).

The role played by the elastic stresses can be demonstrated on the shape of the precipitating particles. In the absence of stress, particles minimize the surface area for the given particle volume and become nearly spherical. In contrast, when the anisotropic elastic stresses are large, the surface energy yields to the stress, and the morphology of particles changes from spherical to cuboidal or elongated shapes such as rectangular or square plates [2]. The changes in particle morphology originates from the fact that the system is governed by two competing energies, (i) one due to the presence of an interface and (ii) the second due to the elastic stresses. If only the interfacial energy is present, an isolated precipitate having isotropic surface energy takes a spherical shape to minimize the interfacial area. When an elastic stress is present, the total energy of the system may be reduced if the shape of the precipitate deviates from the spherical one. Specifically, when there is an anisotropy in the elastic constants, the interface tends to become flat along the elastically soft directions and highly curved along the elastically hard directions. The resulting shapes are cuboidal with rounded corners and nearly flat sides. The energy may be further reduced by changing the aspect ratio of the precipitate, resulting in the plate-like shapes. Such microstructures are seen in many alloy systems, e.g. binary alloys Ni-Al [30] and Ni-Si [31,32]. The exact shape depends on the ratio of the two energies and the degree of the elastic anisotropy of the material. The subject has been widely reviewed in [33–35].

4 Grain boundaries

Grain boundaries constitute a larger and more general class of interfaces in solid state. Unlike, coherent interphase boundaries, GBs break the continuation of the lattice plane across the boundary. One of the major challenges that the study of GBs imposes is the number of macroscopic degrees of freedom required to describe and identify a GB: Three parameters are required to define the lattice misorientation of a GB (3 dimensional phase space). However the aforementioned three degrees of freedom are not enough to fully characterize the coincidence at the boundary of two adjacent grains. Two additional parameters necessary to define the boundary plane inclination are required (2 dimensional phase space). A number of recent reports highlight the importance of the interface inclination on the properties of a GB (see Ref. [76] and Refs therein). Thus, for a complete macroscopic description a five dimensional GBs configurational is necessary.

In the next section we will shortly review the available atomistic approaches to address the grain boundary formation energies γ_{GB} and we will provide recent results based on first principles density functional theory and modified embedded atom method (MEAM) calculations of GBs in Al in order to compare the different simulation techniques.

4.1 Different geometries to model a GB

In atomistic scale simulations of GBs and/or dislocations a common approach to model the extended defect is to perform slab or cluster calculations: In the slab geometry a single defect is placed at the center of the cell and periodicity is applied only for the two directions parallel to the the GB plane (see Fig. 3(b)). On the other hand in the cluster geometry the GB is imposed in a bulk crystal of finite size and no periodic boundary conditions (PBC) are applied to the system (see Fig. 3(c)). If a code which inherently imposes PBC is used caution should be taken for the vacuum thickness d in order to ensure efficient decoupling of the free surfaces: The vacuum thickness should be larger than the range of the interatomic potential or convergence checks should be carefully undertaken in case of e.g. planewave *ab-initio* calculations. Nevertheless, both geometries have the advantage of the absence of a second geometrically necessary compensating defect in order to ensure periodic boundary conditions: The use of periodic boundary

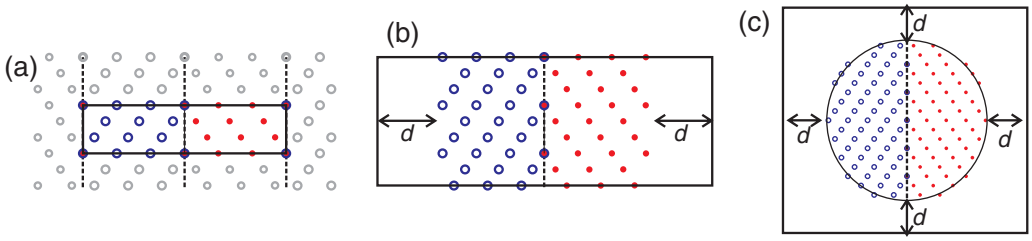

Fig. 3. Schematic representation of the different simulation geometries used to calculate GB formation energies γ_{GB}: (a) Supercell with PBC in all three directions, (b) slab geometry, and (c) cluster geometry. The dashed lines indicate the position of the interfaces while open and filled balls are used to denote atoms located in opposite grains. Gray balls in (a) represent the periodic images of the supercell and d in (b) and (c) denotes the vacuums thickness.

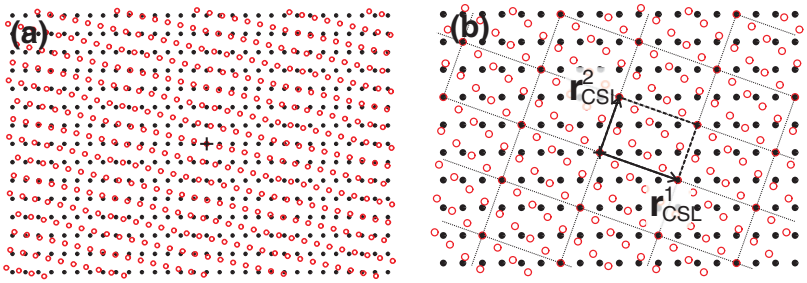

Fig. 4. Moiré patterns formed by the lattice points of two interpenetrating grains denoted by the open and filled balls respectively. The cross denote the position of the [110] rotation axis. Only one of the two (110) planes is shown. (a) For an arbitrary rotation angle (here $\approx 12.70^\circ$) no superlattice is formed. (b) For special rotation angles (here $\approx 38.94^\circ$) a superlattice (the CSL) consisting of the coincident points is formed. The dotted lined indicate the planes of the CSL and the thick dashed lines its unit cell. The unit vectors are also shown. The superlattice shown here is to the $\Sigma 9$ CSL.

conditions requires the existence of a finite size unit cell which has translational symmetry. However, extended defects such as dislocations and GBs break the crystal translational symmetry. This problem is circumvented by forming a second compensating defect[1]. Nevertheless, cluster and slab geometries impose the problem of the free surface treatment: The effect of the free surface on the atomic geometry, electronic structure and total energy of the system under consideration is not known in advance. Moreover different grain boundary misorientations impose different free surfaces. Thus, even the relative comparison of two defects is a puzzling situation.

An alternative approach which is aimed to eliminate the surface effects uses three dimensional periodic boundaries conditions with supercells which have a pair of compensating defects (see Fig. 3(a)). The defect-defect interactions are assumed to be negligible if the separation distance is taken to be sufficiently large. However, for *ab-initio* calculations the size of the systems which may be handled is of the order of few hundreds of atoms. Thus, first principles calculations are suitable to describe GB systems of only special misorientation and inclination. On the other hand empirical or semi-empirical potentials may handle systems consisting of more than a few hundreds of thousands or even millions of atoms and various misorientations and inclinations can be addressed (see e.g. Ref. [88]).

4.2 Coincidence Site Lattice

In order to construct a supercell containing a pair of compensating GBs the symmetry of the crystal has to be explicitly taken into account. In principle there is an infinite number of possible

[1] The analogous in electrostatics is if we assume the extended defect as a charged entity to place a compensating charge of opposite sign in order to assess charge neutrality.

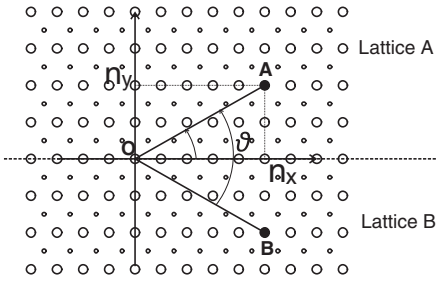

Fig. 5. Schematic representation of the construction of a CSL for rotation on the (110) fcc plane. The rotation [110] axis is at the origin of the frame of reference (point **O**). Large and small balls denote atoms in the two successive (110) fcc planes. We assume two lattices, Lattice A and Lattice B, which initially are in full coincidence. Only the upper (lower) half of Lattice A (B) are shown respectively.

misorientations of two grains relative to each other. However due to symmetry reasons and the discrete nature of the lattice, it is not possible each of them to be included in a supercell with its compensating image. In order to tackle this problem the concept of the Coincidence Site Lattice (CSL) is used: Let us consider the Moiré pattern formed by the lattice points of two interpenetrating grains with the same origin which the one has been rotated relative to the other. For an arbitrary misorientation angle the Moiré pattern will look like the one in Fig. 4(a). However, for certain special rotation angles some lattice points from both grains will coincide and a superlattice, the CSL, will be formed (see Fig. 4(b)). The CSL has a certain translational symmetry defined by the CSL primitive vectors ($\mathbf{r}^1_{CSL}$ and $\mathbf{r}^2_{CSL}$ in the 2D example of Fig 4). The ratio of the unit cell volume of the CSL to the unit cell volume of the regular lattice corresponds to the Σ value of the CSL. In can be shown that the numerical value of Σ is always odd [70]. $\Sigma 1$ CSL would denote a perfect crystal, i.e. the lack of any boundary. Nevertheless, low angle GBs, e.g. GBs that are composed by a superposition of an array of lattice dislocations and have misorientation angles smaller than $\simeq 10 - 15°$, are also commonly referred as $\Sigma 1$ boundaries.

Once the CSL and hence the Σ value is defined the three macroscopic degrees of freedom associated with the misorientation of the grains are uniquely defined. The other two degrees of freedom associated with the boundary inclination can be assessed by choosing various CSL planes, i.e. planes that intersect CSL points. The advantage of the CSL concept is that thanks to its translational symmetry any two parallel CSL planes would correspond to two identical GBs. Therefore, a supercell a pair of equivalent GBs with certain misorientation and inclination can be formed in the following way: In a first step the corresponding CSL is constructed. Although not all GBs are CSL boundaries, any GB can be approximated by a CSL boundary of arbitrary large Σ value and very close misorientation angles. A detailed description on the construction of a CSL can be found in Ref. [70]. Nevertheless, as an example we demonstrate the construction of a CSL of tilt GBs in fcc crystals having as rotational axes the [110] axes (see Fig. 5): We assume two lattices, Lattice A and Lattice B, which initially are in full coincidence. Only the upper half of Lattice A and the lower half of Lattice B are shown in Fig. 5. In order to construct a CSL, Lattice B has to be rotated by an angle θ which will bring sites of Lattice B to coincide with sites of Lattice A. In order for example to bring point **B** ontop of point **A**, Lattice B should be rotated by an angle $\theta = 2\arctan((n_y \mathbf{r}_y)/(\mathbf{r}_x n_x))$, where n_x and n_y are lattice coordinates and $\mathbf{r}_x$ and $\mathbf{r}_y$ the corresponding fcc lattice vectors. The vector $\mathbf{r}_{OA} = n_x \mathbf{r}_x + n_y \mathbf{r}_y$ will be one of the three CSL primitive vectors. The second CSL primitive vector is the fcc lattice vector along the [110] direction. The third one is the normal to the $\mathbf{r}_{OA}$ lying in the (110) plane.

Once the CSL has been constructed and the misorientation has been fixed, the boundary plane has to been chosen. In principle an infinite number of boundary planes exists for a given CSL. However, it is expected that boundaries that contain higher density of lattice points in a CSL is expected to exhibit better atomic fit and therefore more pronounced cohesion. The density of atomic points at the boundary is inverse proportional to both the Σ value and the area of the 1×1 boundary unit cell. Once the boundary plane is chosen, the supercell can be

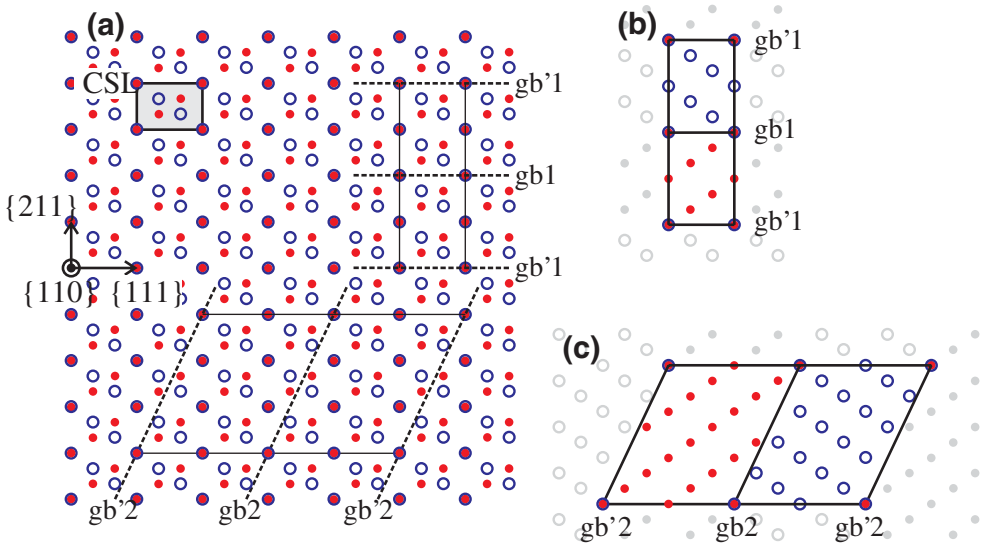

Fig. 6. Schematic representation of a procedure to construct various GBs for a given CSL. Open and filled balls correspond to atoms of two different grains. Grey balls denote the periodic images of the atoms. (a) Each CSL plane corresponds as those denoted by the dashed lines corresponds to a GB with a misorientation defined uniquely by the Σ value. Any two parallel CSL planes correspond to GBs having the same inclination (e.g. gb1 and gb'1 as well as gb2 and gb'2). (b) and (c) Supercells containing a pair of compensating GBs.

constructed by choosing two additional planes parallel to the first one, as schematically shown in Fig. 6.

However besides the five macroscopic degrees of freedom there is in principle an infinite number of microscopic degrees of freedom which control the free energy and the cohesive properties of a GB. These degrees of freedom correspond to translations of the one grain with respect to the other, boundary expansion or "breathing" of the boundary (excess volume), and the coordinates of the atoms in boundary and at the neighborhood of the boundary. While the atomic positions can be implicitly derived by performing atomic relaxation, the other microscopic degrees of freedom have to explicitly taken into account by applying the corresponding translations to the one of the two grains.

4.3 GB energies: Discussion

In Fig. 7(a) the energies for symmetrical tilt [110] GBs in Aluminum derived by MEAM and *ab-initio* supercell calculations are shown [73]. The energy profile extends in the range of 0° to 180° of misorientation angles and has a few cusps which correspond to low low Σ value CSL. An interesting finding is that the MEAM potential calculations describe the energetics of GBs within 10% with respect to the *ab-initio* calculated energies, which is an indication that the Al modified EAM potential used here, describes the interatomic interactions fairly well. Unfortunately only relative experimentally measured GB energies for the [110] symmetrical tilt GBs in Al are available in the literature [74]. Thus, only qualitative comparisons can be made. Indeed our results closely reproduce the energy profile of the experimentally accessible energies.

The great advantage of constructing the GB based on the CSL concept is that all the GBs are formed by pure symmetry operations. Thus, the use of periodic boundary conditions restricts the interface planes to have the area and the misorientation defined by the aforementioned symmetry operations. Consequently, the interface area and the interface reconstruction are known in advance. Moreover, the possibility of the boundary plane to reconstruct according to the Wulff-Herring reconstruction [67,68] is rather limited and, in principle, GBs with the exact

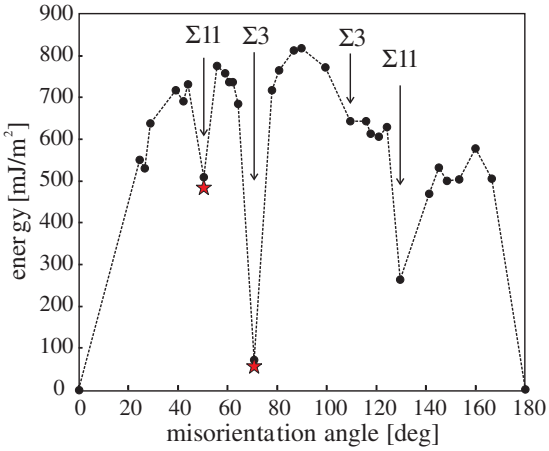

Fig. 7. Computed symmetrical tilt GB energies for Al as function of the misorientation having the [110] rotational axis. Disks (stars) denote the MEAM (*ab-initio*) calculated energies respectively.

assumed misorientation and/or inclination are calculated. This is contrast cluster calculations: B. J. Lee et al. [75] have been calculated the [110] symmetrical tilt GBs implementing large spherical clusters having 8 to 10 nm diameter. They have calculated on average 100 mJ/m^2 lower interfacial energies which can be attributed to heavy interfacial reconstructions. Moreover, the reported that an error bar of approximately 60 mJ/m^2 originated from the estimation of the free surface energies should be added to the cluster derived formation energies. Nevertheless, the cluster approach provides the advantage that the 5D space of grain boundary misorientations and inclinations can be assessed in a continuous manner. Moreover along with the slab calculations, thanks to the lack of translational symmetry restrictions to directions normal to the boundary, smaller cells can be used for arbitrary GBs.

GB energies constitute important input variables for phase field simulations. However, theoretical works that will provide a complete a consistent description of the GB energies as function of the 5 degrees of freedom are still lucking. Recently Olmsted et al. have been reported EAM calculations on 388 CSL GBs which could be constructed in a cell of prescribed size. Slab geometries were utilized and the Σ385 was the largest CSL used [88]. Other reports based on empirical potential calculations have addressed only one of the five degrees of freedom associated with the GBs such as the [110] symmetrical tilt GBs in Al [75,77]. On the other hand, *ab-initio* calculations have been used with great success to describe GBs of certain misorientation and inclination (single point in the 5D configurational space) [78,79,82]. The formation of vacancies, the precipitation of impurities as well as GB sliding and migration have been successfully addressed by first principles calculations [80,81,83–85]. In principle one may conclude that first principle methods are restricted to rather small systems sizes and thus special GBs, they are more suitable to provide an insight understanding of the atomistic mechanisms governing the properties of GBs. A profound example is the investigation of Bi embrittlement of Cu by Schweinfest et al. [84]. On the other hand empirical potential calculations are suitable to provide vast data of GB energies and boundary excess volumes which are a prerequisite in phase field simulation.

5 Solid-liquid interfaces

Mesoscale phase field simulations are an ideal method to describe the evolution of a system during grain and/or dendritic growth. However, the dendritic evolution and solidification processes depend strongly on material specific parameters such as the solid-liquid interfacial free energy γ and the kinetic coefficient μ. Although the dependence of γ on the interface normal $\hat{n}$ is rather low, while that of the μ is one order of magnitude larger, both anisotropies

substantially influence the growth evolution and morphology. Therefore the accurate determination of both parameters constitutes both a challenge as well as a bottleneck for accurate phase field simulations: Experimental precise estimation of the anisotropy of both parameters is extremely difficult, if possible at all. Therefore, a variety of techniques based on Valence Force Field Molecular Dynamics simulations have been developed over the last two decades aiming to provide a accurate estimation of the anisotropy of interfacial free energy and kinetic coefficient. In the following two subsections we will first describe the available techniques proposed to calculate solid-liquid interfacial free energies and then the models to calculate the kinetic coefficient from atomistic calculations.

The solid liquid free energy γ_{SL} corresponds to the revisable work required to form an interface between a crystal and its coexistent melt. Experimentally the value of γ_{SL} can be measured by contact angle experiments: The interfacial free energy is derived by equilibrating the forces at the intersection of crystal, liquid, and grain boundary surfaces. This approach has been applied to various material systems, and although it is relatively accurate it suffers from various approximations and sources of uncertainty (e.g. see Ref. [39]). A less accurate method to derive SL interfacial free energies is based on the measurement of crystal nucleation rates: According to nucleation theory the temperature of critical supercooling depends strongly on and it is directly related to γ_{SL}. However this technique suffers from approximations inherent to classical nucleation theory as well as from purity and homogeneity problems. Moreover, it is not capable to provide the anisotropy of γ_{SL}: The measured interfacial energy is an average over all the orientations.

5.1 Thermodynamic integration

Over the last decades three different techniques based on atomistic calculations have been developed and applied to calculate the interfacial free energy γ_{SL}: In the first category the interfacial energy is directly derived by thermodynamic integration over revisable paths undertaken in order to construct the SL interface from bulk crystal and bulk liquid samples prepared at the calculated temperature and densities [36,38]. The corresponding paths proposed by Broughton and Gilmer [38] are shown in Fig. 8: In a first step an appropriate cleavage potential is inserted in the bulk crystal while PBC along all directions are maintained. In the second step the cleavage of the bulk liquid follows in a similar way. In the third step the crystal and liquid slabs produced are juxtaposed. During this step the cleavage potentials are maintained but the size of the system along the transverse to the interface direction is changed. In the final step the cleavage potential is removed. The energy E of the system at each path is a function of coupling parameter λ which varies over the range 0 to 1. The former value corresponds to the start while the later to the end of the path. The change in the Helmholtz free energy during each step i is calculated via thermodynamic (λ) integration:

$$\Delta E_i^{\mathrm{Hel}} = \int_0^1 \left\langle \frac{\delta E_i}{\delta \lambda} \right\rangle \delta\lambda. \tag{5}$$

The magnitude $\langle \delta E_i/\delta\lambda \rangle$ is evaluated for different λ values at each step. The dependence of the energy on the coupling parameter $E_i(\lambda)$ contains the contributions both from the interatomic potential ϕ_{int} as well as the cleavage potential ϕ_{cl}. At the first step has for example the following form:

$$E_1(\lambda) = \left\langle \sum_{k<l} \phi_{\mathrm{int}}(r_{kl}) + \lambda \sum_{l} \phi_{\mathrm{cl}}(x_l, y_l, z_l) \right\rangle, \tag{6}$$

where the sums are evaluated over the atoms k and l. For the bulk crystal system a purely repulsive and short ranged potential was used. For the bulk liquid special care was taken in order to avoid first order hysteresis phenomena and attractive tails were added to the cleavage potential. Due to zero pressure conditions during the integration paths, the excess Gibbs interface free energy is simply the sum of the calculated Helmholtz free energies over the four steps. In more recent works Davidchak and Laird performed the same integration paths for a hard

sphere [36] and Lennard-Jones model systems [37]. However, instead of of cleavage potentials they used purely repulsive cleavage walls and the interfacial free energy was calculated in terms of average pressure $P(\lambda)$ acting on these walls during each path: $w = \int_0^1 P(\lambda)d\lambda$. The advantage of the cleavage wall proposed by Davidchak and Laird compared to the cleavage potential proposed by Broughton and Gilmer is that in the former case the authors constructed the corresponding walls in order these to introduce minimal perturbation in the system. Although, the Broughton and Gilmer approach suffers from larger statistical uncertainties, both reports based on hard-spheres predicted the following anisotropy with respect to interfacial orientation: $\gamma_{100} < \gamma_{111} < \gamma_{110}$. However, the later work on a continuous Lennard-Jones system by Davidchak and Laird predict a different anisotropy $\gamma_{111} < \gamma_{110} < \gamma_{100}$, which is in agreement with experimental observations on the Al-Cu alloy system [52].

5.2 Atomic density functional theory

Although not purely atomistic it is worth mentioning here an approach which is based on atomic Density Functional Theory based calculations: The interfacial energy is derived by minimization of the atomic density functional $\Omega[\rho]$ which corresponds to the grand canonical free energy of the system [40,60]:

$$\Omega[\rho] = F[\rho] - \mu \int d\mathbf{r}\rho(\mathbf{r}) + \int d\mathbf{r}\rho(\mathbf{r})V_{\text{ext}}(\mathbf{r}), \tag{7}$$

where $F[\rho]$ is the Helmholtz free energy of the system, $\rho(\mathbf{r})$ the atomic density, and $V_{\text{ext}}(\mathbf{r})$ an external potential. The equilibrium density $\rho_0(\mathbf{r})$ is found by minimizing $\Omega[\rho]$:

$$\left| \frac{\delta\Omega}{\delta\rho(\mathbf{r})} \right|_{\rho(\mathbf{r})=\rho_0} = 0. \tag{8}$$

The Helmholtz free energy functional contains two contributions: The first one is an ideal gas part and accounts for the entropic effects during crystallization (F_{id}) while the second one is due to the interatomic interactions F_{exc}. The ideal gas part depends on the temperature T, the atomic density $\rho(\mathbf{r})$, and the thermal wavelength Λ: $F_{\text{id}} = k_{\text{B}}T \int d\mathbf{r}\rho(\mathbf{r})\{\ln[\rho(\mathbf{r})\Lambda^3 r]\}$. The explicit form of F_{exc} is not known and various approximations have been proposed in the past. Ramakrishnan and Youssouff [53] and Haymet and Oxtoby [54] proposed a perturbative approach where the interaction part is expanded about that of the homogenous liquid $F_{\text{ext}}(\rho_l)$ in powers of the crystal and liquid density differences $\Delta\rho(\mathbf{r}) = \rho_s(\mathbf{r}) - \rho_l$:

$$F_{\text{exc}}\left[\rho_s\left(\mathbf{r}\right)\right] = F_{\text{exc}}\left(\rho_l\right) - c^{\{1\}}\left(\rho_l\right) \int d\mathbf{r}\Delta\rho\left(\mathbf{r}'\right) - \frac{1}{2}\int d\mathbf{r}d\mathbf{r}' c^{\{2\}}\left(\mathbf{r}' - \mathbf{r}; \rho_l\right)\Delta\rho\left(\mathbf{r}\right)\Delta\rho\left(\mathbf{r}'\right). \tag{9}$$

Here $c^{\{1\}}(\rho_l)$ is the chemical potential for the liquid phase and $c^{\{2\}}(\mathbf{r}' - \mathbf{r}; \rho_l)$ is the direct Ornstein-Zernike correlation function of the liquid. The functional expansion of Eq. (9) is exact in the $\Delta\rho(\mathbf{r}) \ll 1$ limit. Haymet and Oxtoby introduced an additional square gradient term (Square Gradient Approximation, SGA) for the variation of the density along the interface. An alternative approach proposed by Curtin and Ashcroft [55,56] which lifts the perturbative character of Eq. (9) and provides a more consistent description of the rapidly varying crystal density makes use of a weighted density $\bar{\rho}(\mathbf{r}) = \int d\mathbf{r}' w(|\mathbf{r} - \mathbf{r}'|, \bar{\rho}(\mathbf{r}))\rho(\mathbf{r}')$. This approximation is named Weighted Density Approximation (WDA) and the weight function $w(|\mathbf{r} - \mathbf{r}'|, \bar{\rho}(\mathbf{r}))$ is normalized and chosen in such a way that the liquid structure factor is reproduced in the limit of uniform density. A modification to the WDA which offers a more realistic approximation to the free energy functional has been later proposed by Ohnesorge et al. which is based on a Gaussian approximation for the local atomic density [58]. The atomic DFT approximation has been applied to Solid-Liquid interfacial studies of only model hard-sphere and/or Lennard-Jones systems [58–61].

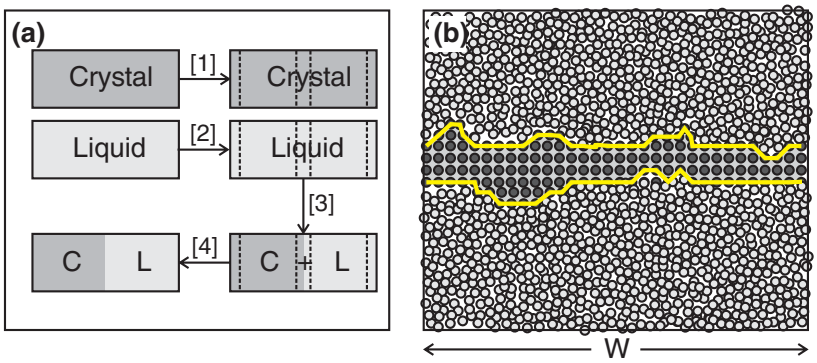

Fig. 8. Schematic representation of the techniques and geometries used to simulate a Crystal-Liquid interfaces: (a) Reversible paths to form a Crystal–Liquid interface. The number in brackets denote the corresponding steps while the dashed line the position of the cleavage potentials (see text). (b) Simulation box for the CFM. Lighter (darker) balls denote to particles in the liquid (solid) phase respectively and the thick line the solid–liquid boundary. Periodic boundary conditions are applied in all three dimensions. W is the length of the cell along the long ribbonlike solid slab.

5.3 Capillary Force Method

More recently an approach which is based on the capillary force calculations has been proposed by Hoyt, Asta, and Karma. The Capillary Force Method (CFM) is based on the calculation of the interfacial stiffness $\gamma + \gamma''$ instead of the interfacial free energy γ, where $\gamma'' \equiv d^2\gamma/d\theta^2$ and θ is the angle between the interfacial normal and the [100] direction. The great advantage of this method is that the interfacial stiffness is by one order of magnitude more anisotropic than the interfacial energy and therefore is much more easier to be computed. In order to determine the interfacial free energy with respect to crystal orientation the former is expanded in terms of cubic harmonics:

$$\frac{\gamma(\hat{n})}{\gamma_0} = 1 + \epsilon_1 \left(\sum_i n_i^4 - \frac{3}{5} \right) + \epsilon_2 \left(3 \sum_i n_i^4 + 66 n_1^2 n_2^2 n_3^2 - \frac{17}{7} \right), \tag{10}$$

where $\hat{n}$ is the interfacial normal, γ_0 is the averaged value of γ, and ϵ_1 and ϵ_2 are the strengths of the fourfold and sixfold anisotropies respectively. The calculation of the γ_0, ϵ_1, and ϵ_2 is based upon the known fact that the interfacial stiffness can be related to the spectrum of interfacial fluctuations in thermodynamic equilibrium. Two different geometries corresponding to a quasi-1D and a 2D interfaces have been used to derive the interfacial fluctuations: Hoyt et al. assumed a ribbonlike interface which is schematically shown in Fig. 8(b). A crystal slab is inserted into a liquid bath forming two SL interfaces. The crystal slab has a ribbonlike morphology: If b and W are the dimensions of the cell parallel to the interface then is assumed that $b \ll W$. This geometry simulates a rather quasi-1D interface. In a subsequent report Becker et al. extended the aforementioned approach to include 2D interfaces (the dimensions of b and W being comparable). The advantage of the quasi-1D over the 2D interfacial system is that in the former the amplitude of the interfacial fluctuations is larger and smaller simulation cells can be employed. However, in the later case smaller number of simulations are required in order to fit the γ, ϵ_1, and ϵ_2 parameters. The height of the fluctuations $h(\mathbf{r})$ can be written in a Fourier series: $h(x_1, x_2) = \sum_{k_1,k_2} A(k_1, k_2) \exp(i(k_1 x_1 + k_2 x_2))$ and the mean square amplitude $\langle |A(k_1, k_2)|^2 \rangle$ can be written as function of the interfacial stiffness:

$$\langle |A(k_1, k_2)|^2 \rangle = \frac{k_B T_M}{A\left(S_{11} k_1^2 + S_{22} k_2^2 + 2 S_{12} k_1 k_2\right)}, \tag{11}$$

where T_M is the melting temperature, A is the cross sectional area of the simulation cell, and (S_{ij}) is a 2×2 stiffness tensor. In order to locate the interface an atomic order parameter ϕ is used: Hoyt et al. assumed for an fcc system as an order parameter the sum of distances over the 12 nearest neighbors: $\phi = \frac{1}{12} \sum_i |\mathbf{r}_i - \mathbf{r}_{fcc}|^2$, which is always positive having values larger than one for the liquid phase and vanishes for the ideal fcc crystal. Morris *et al.* defined a set of N_q vectors such that $\exp(i\mathbf{q} \cdot \mathbf{r}) = 1$ for any vector $\mathbf{r}$ connecting nearest neighbors in an ideal fcc lattice [50]. The order parameter is then defined as $\phi = |\frac{1}{N_q} \frac{1}{Z} \sum_{\mathbf{r}} \sum_{\mathbf{q}} \exp i\mathbf{q} \cdot \mathbf{r}|^2$ which has the value of one for ideal fcc crystal and smaller than one otherwise. In both cases the order parameter changes rapidly as the solid liquid interface is traversed and thus the later can be easily located.

The CFM has been applied to various single component metallic systems such as Ni [42], Au [43], Ag [43], and Al [50] utilizing embedded atom type potentials. Moreover model interactions such as Lennard-Jones [51] interatomic potentials and hard-spheres [49] has been also been used. Nevertheless, studies focusing on crystal-liquid alloy systems are fewer and are restricted to Ni-Cu [44] and Lennard-Jones [46,47] alloys: Although alloys are of high interest for technological applications, the number of available interatomic potentials suitable for multicomponent systems is rather limited.

A detailed discussion on the aforementioned methods to calculate Solid-Liquid interfacial energies and kinetic parameters can be found in the extensive and comprehensive review by Hoyt et al. in Ref. [45]. Nevertheless it is worth to stress here advantages and disadvantages of these techniques. The cleavage approach has the advantage of being computationally more efficient: Almost one order of magnitude larger simulation cells are required for the CFM. Both, the cleavage technique and the CFM, approaches predict anisotropic Solid-Liquid interfacial energies and qualitatively they provide the same results. However, the CFM is based on the calculation of the interfacial stiffness which is by one order of magnitude more anisotropic than the interfacial energy. Thus, the anisotropy in γ is more precisely provided by the CFM.

6 Summary

To summarize, *ab-initio* electronic-structure calculations and/or classical atomistic-modeling approaches are suitable tools which can provide accurate material-specific parameters necessary for state-of-the-art phase field simulations of the mesoscale microstructure evolution. The importance of the atomic-level approaches is closely linked to the fact that many phase-field input parameters can not be directly accessible by experiment. Moreover, in order to control the microstructural evolution, an insight and deeper understanding of various phenomena at the atomic scale are required. Thus, concepts which will allow for a full determination (and thus a possible control over) of all system parameters would be desirable. Obviously, in the ladder of simulation-relevant scales both first-principles and atomistic modeling lie below the phase field simulations. Fortunately, all the three simulation classes may, in principle, be combined in a multi-disciplinary manner into an efficient computational scheme.

In order to do design and apply such a complex modeling approach, a number of hurdles must be overcome. For example, first-principles calculations are on one hand advantageously free of empirical or fitting parameters (what makes them easily transferable into different environment and/or applicable to multicomponent alloys), on the other hand they are suffering from extensive computational requirement what restricts them to rather small system sizes ranging up to a few nanometers. Complementarily, the atomistic modeling can be extended to larger length and time scale but its transferability and accuracy should always be checked and ensured in advance. Also methodologically there are many challenges, as e.g. multidimensional phase space of the interfacial misorientation degrees of freedom, suitable driving forces, and/or large length and time scales, that must be tackled. As the present report shows, the state-of-the-art modeling approaches systematically address these problems and the prospectives to find suitable solutions are very encouraging.

References

1. N. Moelans, B. Blanpaina, P. Wollantsa, Calphad **32**, 268 (2008)
2. V. Vaithyanathan, L.Q. Chen, Acta Mater. **50**, 4031 (2002)
3. K. Thornton, J. Agren, P.W. Voorhees, Acta Mater. **51**, 5675 (2003)
4. Y.W. Lee, H.I. Aaronson, Acta Metall. **28**, 539 (1980)
5. R. Kikuchi, J.W. Cahn, Acta Metall. **27**, 1337 (1979)
6. M.D. Asta, in *Theory and application of the cluster and path probability methods*, edited by J.L. Moran-Lopez and J.M. Sanchez (New York Plenum, 1996), p. 237
7. W. Cao, J. Zhu, F. Zhang, W.A. Oates, M. Asta, Y.A. Chang, Acta Mater. **54**, 377 (2006)
8. W.A. Oates, F. Zhang, S. Chen, Y.A. Chang, Phys. Rev. B **59**, 11221 (1999)
9. W. Cao, Y.A. Chang, J. Zhu, S. Chen, W.A. Oates, Acta Mater. **53**, 331 (2005)
10. W. Cao, J. Zhu, Y. Yang, F. Zhang, S.-L. Chen, W.A. Oates, Y.A. Chang, Acta Mater. **53**, 4189 (2005)
11. P. Cenedese, in *Theory and application of the cluster and path probability methods*, edited by J.L. Moran-Lopez, J.M. Sanchez (New York Plenum, 1996), p. 247
12. M. Asta, Acta Mater. **44**, 4131 (1996)
13. W. Cao, J. Zhu, Y. Yang, F. Zhang, S. Chen, W.A. Oates, Y.A. Chang, Acta Mater. **53**, 4189 (2005)
14. M. Asta, J.J. Hoyt, Acta Mater. **48**, 1089 (2000)
15. C.P. Flynn, *Point defects and diffusion* (London: Clarendon Press, 1972)
16. A. van de Walle, M. Asta, P.W. Voorhees, Phys. Rev. B **67**, 041308 (2003)
17. J.W. Cahn, Acta Metall. **10**, 789 (1962)
18. H. Emmerich, *The Diffuse Interface Approach in Materials Science* (Springer, Lecture Notes in Physics LNPm, 2003), p. 73
19. H. Emmerich, Cont. Mech. Thermodynamics **15/2**, 197 (2003)
20. R. Folch, M. Plapp, Phys. Review E **72**, 1 (2005)
21. A.G. Khachaturyan, *Theory of structural transformations in solids* (New York, Wiley, 1983)
22. Y. Wang, L.Q. Chen, A.G. Khachaturyan, in *Computer Simulation in Materials Science,* edited by H.O. Kirchner, L. Kubin, V. Pontikis (1995), p. 32
23. M. Friák, M. Šob, V. Vitek, Phys. Rev. B **63**, 052405 (2001)
24. M. Friák, A. Schindlmayr, M. Scheffler, New J. Phys. **9**, 5 (2007)
25. M. Friák, W.A. Counts, D. Raabe, J. Neugebauer, Phys. Stat. Sol. b **245**, 2636 (2008)
26. W.A. Counts, M. Friák, C.C. Battaile, D. Raabe, J. Neugebauer, Phys. Stat. Sol. b **245**, 2630 (2008)
27. W.A. Counts, M. Friák, D. Raabe, J. Neugebauer, Acta Mater. **57**, 69 (2009)
28. M. Friák, J. Deges, F. Stein, M. Palm, G. Frommeyer, J. Neugebauer, in *Advanced Intermetallic-Based Alloys for Extreme Environment and Energy Applications*, edited by M. Palm, B.P. Bewlay, M. Takeyama, J.M.K. Wiezorek, Y.-H. He (Mater. Res. Soc. Symp. Proc. **1128**, Warrendale, PA, 2009), 1128-U02-04
29. D. Ma, M. Friák, D. Raabe, J. Neugebauer, F. Roters, Phys. Stat. Sol. b **245**, 2642 (2008)
30. A.J. Ardell, R.B. Nicholson, Acta Metall. **14**, 1295 (1966)
31. J. Cho, A. Ardell, Acta Mater. **45**, 1393 (1997)
32. J.H. Cho, A.J. Ardell, Acta Mater. **46**, 5907 (1998)
33. M. Doi, Mater. Trans. JIM **33**, 637 (1992)
34. P.W. Voorhees, Annu. Rev. Mater. Sci. **22**, 197 (1992)
35. P. Fratzl, O. Penrose, J. Lebowitz, J. Stat. Phys. **95**, 1429 (1999)
36. R.L. Davidchack, B.B. Laird, Phys. Rev. Lett. **85**, 4571 (2000)
37. R.L. Davidchack, B.B. Laird, J. Chem. Phys. **118**, 7651 (2003)
38. J.Q. Broughton, G.H. Gilmer, J. Chem. Phys. **84**, 5759 (1986)
39. D.P. Woodruff, *The solid-liquid interface* (CUP Archive, Cambridge, 1973), p. 12
40. W.E. McMullen, D.W. Oxtoby, J. Chem. Phys. **88**, 1967 (1988)
60. W.A. Curtin, Phys. Rev. B **39**, 6775 (1989)
42. J.J. Hoyt, M. Asta, A. Karma, Phys. Rev. Lett. **86**, 5530 (2001)
43. J.J. Hoyt, M. Asta, Phys. Rev. B **65**, 214106 (2002)
44. J.J. Hoyt, M. Asta, A. Karma, Phys. Rev. B **66**, 100101(R) (2002)
45. J.J. Hoyt, M. Asta, Mater. Sci. Eng. R **41**, 121 (2003)
46. C.A. Becker, D. Olmsted, M. Asta, J.J. Hoyt, S.M. Foiles, Phys. Rev. Lett. **98**, 125701 (2007)
47. C.A. Becker, D. Olmsted, M. Asta, J.J. Hoyt, S.M. Foiles, Phys. Rev. B **79**, 054109 (2009)

48. C.A. Becker, M. Asta, J.J. Hoyt, S.M. Foiles, J. Chem. Phys. **124**, 164708 (2006)
49. R.L. Davidchack, J.R. Morris, B.B. Laird, J. Chem. Phys. **125**, 094710 (2006)
50. J.R. Morris, Phys. Rev. B **66**, 144104 (2002)
51. J.R. Morris X. Song, J. Chem. Phys. **119**, 3920 (2003)
52. S. Liu, R.E. Napolitano, R. Trivedi, Acta Mater. **49**, 4271 (2001)
53. T.V. Ramakrishnan, M. Yussouff, Phys. Rev. B **19**, 2775 (1979)
54. A.D.J. Haymet, D.W. Oxtoby, J. Chem. Phys. **74**, 2559 (1981)
55. W.A. Curtin, N.W. Ashcroft, Phys. Rev. A **32**, 2909 (1985)
56. W.A. Curtin, N.W. Ashcroft, Phys. Rev. Lett. **56**, 2775 (1985)
57. Y.C. Shen, D.W. Oxtoby, J. Chem. Phys. **104**, 4233 (1995)
58. R. Ohnesorge, H. Lowen, H. Wagner, Phys. Rev. A **43**, 2870 (1991)
59. R. Ohnesorge, H. Lowen, H. Wagner, Phys. Rev. E **50**, 4801 (1994)
60. W.A. Curtin, Phys. Rev. B **39**, 6775 (1989)
61. W.E. McMullen, D.W. Oxtoby, J. Chem. Phys. **88**, 1967 (1987)
62. T. Watanabe, Res. Mech. **11**, 47 (1984)
63. G. Palumbo, International Patent Publication WO 94/14986, World Intellectual Property Organization, Geneva, Switzerland, allowed August 1996
64. G. Palumbo, P.J. King, K.T. Aust, U. Erb, P.C. Lichtenberger, Scripta Metall. Mater. **25**, 1775 (1991)
65. D.M. Saylor, B.S. El Dasher, A.D. Rollett, G.S. Rohrer, Acta Materialia **52**, 3649 (2004)
66. B.J. Lee, J.H. Shim, M.I. Baskes, Phys. Rev. B **68**, 144112 (2003)
67. G. Wulff, Z. Kristallogr. Mineral. **34**, 449 (1901)
68. C. Herring, Phys. Rev. **82**, 87 (1951)
69. A.P. Sutton, R.W. Balluffi, *Interfaces in Crystalline Materials* (Oxford Science publications, Clarendon Press, Oxford, 1995)
70. W. Bollmann, *Crystal Defects and Crystalline Interfaces* (Springer-Verlag, 1970)
71. R.G. Parr, W. Yang, *Density Functional Theory of Atoms and Molecules* (Oxford Science Publications, Clarendon Press, Oxford, 1989)
72. K. Ohno, K. Esfarjani, Y. Kawazoe, *Computantional Materials Science*, Springer Series in Solid-State Sciences (Springer, Oxford, 1999)
73. L. Lymperakis, J. Neugebauer (in preparation)
74. G.C. Hasson, C. Goux, Scripta Metall. **5**, 889 (1971)
75. B.J. Lee, S.H. Choi, Modeling Simul. Mater. Sci. Eng. **12**, 621 (2004)
76. C.-S. Kim, A.D. Rollett, G.S. Rohrer, Scripta Mater. **54**, 1005 (2006)
77. S.R. Nishitani, S. Ohgushi, Y. Inoue, H. Adachi, Mater. Sci. Eng. **A309–490** (2001)
78. M.C. Payne, P.D. Bristowe, J.D. Joannopoulos, Phys. Rev. Lett. **58**, 1348 (1987)
79. M. Needels, A.M. Rappe, P.D. Bristowe, J.D. Joannopoulos, Phys. Rev. B **46**, 9768 (1992)
80. T.A. Arias, J.D. Joannopoulos, Phys. Rev. B **49**, 4525 (1994)
81. C. Molteni, G.P. Francis, M.C. Payne, V. Heine, Phys. Rev. Lett. **76**, 1284 (1996)
82. A.F. Wright, S.R. Atlas, Phys. Rev. B **50**, 15248 (1994)
83. G. Lu, N. Kioussis, Phys. Rev. B **64**, 024101 (2001)
84. R. Schweinfest, A.T. Paxton, M.W. Finnis, Nature **432**, 1008 (2004)
85. R. Siegl, M. Yan, V. Vitek, Modelling Simul. Mater. Sci. Eng. **5**, 105 (1997)
86. G. Lu, N. Kioussis, R. Wu, M. Ciftan, Phys. Rev. B. **59**, 891 (1999)
87. S.J. Plimpton, J. Comp. Phys. **117**, 1 (1995) (website: `http://lammps.sandia.gov/index.html`)
88. D.L. Olmsted, S.M. Foiles, E.A. Holm, Acta Material. **57**, 3694 (2009)
89. W. Kohn, L.J. Sham, Phys. Rev. **140**, A1133 (1965)
90. M.P. Umrigar, J. Cyrus J. (eds.), *Quantum Monte Carlo Methods in Physics and Chemistry*, Proceedings of the NATO Advanced Study Institute (Springer, 1998)
91. M. Finnis, E. Sinclair, Phil. Mag. A. **5**, 45 (1984)
92. M.S. Daw, M.I. Baskes, Phys. Rev. Lett. **50**, 1285 (1983)
93. M.S. Daw, S.M. Foiles, M.I. Baskes, Mater. Sci. Reports **9**, 251 (1993)
94. M.I. Baskes, Phys. Rev. Lett. **59**, 2666 (1987)
95. Ş. Erkoç, Phys. Reports **278**, 79 (1997)
96. F.H. Stillinger, T.A. Weber, Phys. Rev. B **31**, 5262 (1985)
97. J.E. Angelo, N.R. Moody, M.I. Baskes, Modelling Simul. Mater. Sci. Engr. **3**, 289 (1995)
98. B.J. Lee, M.I. Baskes, H. Kim, Y.K. Cho, Phys. Rev. B **64**, 184102 (2001)
99. D.J. Hepburn, G.J. Ackland, Phys. Rev. B **78**, 165115 (2008)
100. NIST repository: `http://www.ctcms.nist.gov/potentials`